PHYSICAL REVIEW D **94,** 123012 (2016)

Inferring the core-collapse supernova explosion mechanism with gravitational waves

Jade Powell,[1] Sarah E. Gossan,[2] Joshua Logue,[1] and Ik Siong Heng[1]
[1]*University of Glasgow, Physics and Astronomy, Kelvin Building, Glasgow, Lanarkshire G12 8QQ, United Kingdom*
[2]*LIGO 100-36, California Institute of Technology, Pasadena, California 91125, USA*
(Received 16 October 2016; published 27 December 2016)

A detection of a core-collapse supernova (CCSN) gravitational-wave (GW) signal with an Advanced LIGO and Virgo detector network may allow us to measure astrophysical parameters of the dying massive star. GWs are emitted from deep inside the core, and, as such, they are direct probes of the CCSN explosion mechanism. In this study, we show how we can determine the CCSN explosion mechanism from a GW supernova detection using a combination of principal component analysis and Bayesian model selection. We use simulations of GW signals from CCSN exploding via neutrino-driven convection and rapidly rotating core collapse. Previous studies have shown that the explosion mechanism can be determined using one LIGO detector and simulated Gaussian noise. As real GW detector noise is both nonstationary and non-Gaussian, we use real detector noise from a network of detectors with a sensitivity altered to match the advanced detectors design sensitivity. For the first time, we carry out a careful selection of the number of principal components to enhance our model selection capabilities. We show that with an advanced detector network we can determine if the CCSN explosion mechanism is driven by neutrino convection for sources in our Galaxy and rapidly-rotating core collapse for sources out to the Large Magellanic Cloud.

DOI: 10.1103/PhysRevD.94.123012

I. INTRODUCTION

More than 80 years after Baade and Zwicky first proposed that core-collapse supernovae (CCSNe) are massive stars turning into neutron stars at the end of their life [1], the CCSN explosion mechanism is still not fully understood.

Zero age main sequence (ZAMS) stars with $8\ M_\odot < M < 100\ M_\odot$ form electron-degenerate cores composed primarily of iron-group nuclei in the final stages of their nuclear burning. Once the iron core exceeds its effective Chandrasekhar mass (see, e.g., Refs. [2,3]), it becomes gravitationally unstable. Gravitational collapse continues until the inner core is dynamically compressed to nuclear densities. At this point, the equation of state (EOS) stiffens, the inner core rebounds (typically referred to as *core bounce*), and a shock wave is launched outward from the outer edge of the inner core. The shock suffers energy losses due to the dissociation of infalling iron-group nuclei and neutrino losses from electron capture in the region behind the shock. Yielding to ram pressure due to the outer core, the shock stalls and becomes an accretion shock. If the shock is not revived within ~0.5–3 s, accretion onto the protoneutron star will lead to further gravitational collapse and black hole formation [4]. Understanding how the stalled shock is revived to explode the dying star, the CCSN explosion mechanism, is one of the most important challenges in CCSN theory today.

There is little information on the CCSN explosion mechanism to be gleaned from electromagnetic (EM) observations, as EM emission from CCSNe occurs in optically thin regions, far from the central engine, and so only secondary information on the explosion mechanism is available. Observations of CCSN ejecta and pulsar kicks are indicative of the multidimensional physical processes driving the explosion [5,6].

Gravitational waves (GWs) and neutrinos, however, are emitted from deep inside the core, and, as such, they are direct probes of the CCSN explosion mechanism. While GWs from CCSNe have not yet been directly detected, the few neutrinos detected from SN1987A confirmed the above picture of core collapse [7–9].

The core collapse of massive stars has been considered as a potential source for the Advanced LIGO (aLIGO) and Advanced Virgo (AdVirgo) detectors—see Refs. [10,11] for a historical overview. The aLIGO detectors are laser interferometers with 4 km arms located in Livingston, Louisiana, and Hanford, Washington [12]. AdVirgo is a 3 km Italian detector expected to join the aLIGO detector network early in 2017 [13]. Recent work by Gossan *et al.* [14] shows that GWs from nonrotating and rotating core collapse may be observable throughout the Milky Way and the Large Magellanic Cloud. The rate for these sources is low at around $\lesssim$2–3 CCSNe per 100 years [15–18]. No detections were made in the first targeted search for CCSNe GWs [19].

Numerical simulations have allowed a number of GW emission processes in CCSNe to be identified, including but not limited to rotating core collapse and bounce, rotational instabilities, neutrino-driven convection, prompt convection in the region behind the shock, standing

accretion shock instability (SASI), and asymmetric neutrino emission [10]. The multidimensional processes occurring in CCSNe are incredibly complex, and so even with state of the art simulations, the stochastic nature of many GW emission processes (e.g. convection and turbulence) result in a signal with a stochastic phase that cannot be robustly predicted. In the absence of a robust method to estimate the signal's phase evolution, matched filtering (the optimal signal extraction method for known signal morphology in Gaussian noise [20]) cannot be used. To this end, it is beneficial to associate proposed explosion mechanisms with a set of GW emission processes, such that the broad characteristics of GW signals from each mechanism can be determined. This will allow the detection of GWs from CCSNe to be used to infer the CCSN explosion mechanism.

The first application of numerical GW waveforms for CCSNe to infer the CCSN explosion mechanism was carried out by Logue *et al.* [21] and considered signals from neutrino-driven convection [22], rapidly rotating core collapse [23], and protoneutron star pulsations [24,25] (denoted the neutrino mechanism, magnetorotational mechanism, and acoustic mechanism, respectively). We hereafter refer to this paper as L12. Following previous work by Heng [26] and Röver *et al.* [27], principal component analysis (PCA) [28] was used to create principal component basis vectors (PCs) from the GW signals associated with each explosion mechanism. Linearly polarized signals were added, or "injected," in Gaussian noise with the design sensitivity power spectral density (PSD) of the aLIGO detectors [12], and a Bayesian nested sampling algorithm [29] was used to compute the evidence that the signals were best represented by each PC basis. Comparison of the evidences for a given signal then permitted the most likely explosion mechanism to be identified via model selection. The algorithm used for this analysis was denoted the Supernova Model Evidence Extractor (SMEE).

There were several major limitations to the SMEE analysis. First, signals were injected into data for one detector, assuming optimal orientation and sky location for maximal antenna sensitivity of the detector (see Ref. [14] for information on the antenna sensitivity of an interferometric GW detector). Given this, the time-varying antenna sensitivity for a given detector was not taken into account, and hence the antenna sensitivity considered was artificially optimistic. Additionally, the single detector network chosen did not account for the multiple GW detectors scheduled to come online during the advanced detector era, resulting in limited sensitivity. Further, only GW signals extracted from axisymmetric CCSN simulations were considered, resulting in linearly polarized signals. However, EM observations suggest that many, if not most, CCSN explosions exhibit asymmetric features [30–34]. The 3D magnetorotational simulations for rapidly rotating progenitors show a dominant GW polarization is expected for the bounce signal. However, 3D neutrino mechanism simulations show that the stochastic nature of the asymmetric flow structures arising from the SASI and convection will lead to unpolarized GWs from CCSNe [35–44]. Finally, the use of Gaussian noise meant that the effect of noise transients present in real GW detector noise could not be studied. Despite these limitations, the SMEE algorithm demonstrated the ability to distinguish magnetorotational explosions within the Milky Way ($D \leq 10$ kpc), while neutrino-driven and acoustic explosions could be distinguished for sources closer than $D \leq 2$ kpc. The goal of this second model selection study is to address the shortcomings of the original SMEE analysis and to make more accurate statements on the ability to infer the CCSN explosion mechanism from GW observations of CCSNe in the advanced detector era.

In this paper, we outline the improvements made to the SMEE analysis to address several of the limitations described previously. We consider a three detector network with non-Gaussian, nonstationary detector noise, at multiple GPS times to vary the antenna pattern sensitivity. We continue to use linearly polarized GW waveform catalogs to produce the PCs because, at this time, large waveform catalogs from 3D CCSN simulations do not exist. Further, we do not consider GW signals from the acoustic mechanism in this study, as this is no longer considered a viable explosion mechanism for CCSNe [45].

This paper is structured as follows. In Sec. II, we provide an overview of the CCSN explosion mechanisms considered, the characteristics of the associated GW emission, and the GW waveform catalogs chosen for this study. In Sec. III, we review the method used in SMEE for Bayesian model selection via nested sampling. In Sec. IV, we provide details of the analysis. In Sec. V, we show the results of our study at Galactic and extra-Galactic distances. We summarize and discuss the implications in Sec. VI.

II. CORE-COLLAPSE SUPERNOVA EXPLOSION MECHANISMS AND THEIR GRAVITATIONAL WAVE SIGNATURES

In this section, we consider the magnetorotational mechanism and the neutrino mechanism for driving CCSN explosions. We hereafter provide a broad overview of the physical processes driving the explosion dynamics, in addition to the characteristic features imprinted on the associated GW emission. We direct the reader to L12 for a more in-depth description of the explosion mechanisms.

A. Magnetorotational mechanism

Due to conservation of angular momentum, core collapse to a protoneutron star results in the spin-up of the core by a factor of 1000 [46]. Consequently, rapidly rotating precollapse cores with periods $\sim$1 s form protoneutron stars with periods on millisecond time scales. Such compact objects have rotational energy $\sim 10^{52}$ erg, a small fraction

of which could power a strong CCSN explosion, if somehow tapped.

Theory and simulations have shown that magnetorotational processes efficiently extract rotational energy and may drive collimated outflows in rapidly rotating core-collapse explosions (see, e.g., Refs. [23,47] and references within). Flux compression due to collapse alone cannot produce the magnetic fields required (of order 10^{15} G) for bipolar explosions, given the precollapse core magnetic fields predicted by stellar evolution models [48]. More plausible an explanation is magnetic amplification after core bounce, through rotational winding of the poloidal field into the toroidal field, and the magnetorotational instability, though the latter is not well understood in the context of CCSNe, but some progress toward understanding has been made in recent years [49,50]. For the magnetorotational mechanism to work, simulations suggest that the precollapse core needs spin period $\lesssim$4–5 s [23].

The GW signal from rapidly rotating CCSNe is dominated by the bounce and subsequent ring down of the protoneutron star. Strong centrifugal deformation of the inner core results from a rapidly rotating precollapse core, leading to a large, time-varying quadrupole moment, which consequently sources a strong burst of GWs. It is expected that the precollapse core angular velocity distribution is roughly uniform in the inner core [48], which is preserved in the subsonically collapsing inner core due to homologous collapse. In the supersonically collapsing regions outside the inner core, however, homologous collapse drives strong rotation gradients, causing the outer core and region between the protoneutron star and the shock to be strongly differentially rotating [46]. Due to this, convection is inhibited in these regions, and the GW signature of the turbulent convection characteristic of nonrotating core collapse is not present. For slowly rotating core collapse, prompt convection may contribute to the GW signal on time scales of tens of ms [51,52]. Typically, the peak GW strain from rotating core collapse is $\sim 10^{-21}$–10^{-20} for a source at 10 kpc, and emitted energy in GWs ($E_{\rm GW}$) is $\sim 10^{-10}$–$10^{-8} M_\odot$. The GW energy spectrum is more narrowband than for nonrotating core collapse, with most power emitted between 500–800 Hz, over time scales of a few tens of ms. For precollapse cores with initial spin period less than $\sim 0.5-1$ s, core bounce occurs slowly at subnuclear densities, dynamics are dominated by centrifugal effects, and most energy in GWs is emitted around $\sim$200 Hz [10,51]. It is also possible for nonaxisymmetric rotational instabilities to develop in the protoneutron star, which may source GWs over time scales of hundreds of ms [37–39,53,54].

1. GW waveform catalogs

For the purposes of this study, we draw from the Dimmelmeier *et al.* [51] waveform catalog to construct the magnetorotational mechanism PCs, hereafter referred to as the `RotCC` model. The full catalog, comprised of 128 waveforms, spans progenitor star ZAMS mass ($M_{\rm ZAMS} \in \{12, 15, 20, 40\} M_\odot$), angular momentum distribution, and nuclear matter EOS. The initial angular momentum distribution of the precollapse core is imposed through a parametrized angular velocity profile, $\Omega_i(\bar{\omega})$, defined as

$$\Omega_i(\bar{\omega}) = \frac{\Omega_{c,i}}{1 + (\bar{\omega}/A)^2}, \tag{1}$$

where $\bar{\omega}$ is the cylindrical radius, $\Omega_{c,i}$ is the central angular velocity, and A is the differential rotation length scale. Simulations are performed across the angular momentum distribution space, considering strongly differential rotation ($A = 500$ km) to almost uniform rotation ($A = 50\,000$ km) and slowly rotating ($\Omega_{c,i} = 0.45$ rad s^{-1}) to rapidly rotating ($\Omega_{c,i} = 13.31$ rad s^{-1}) precollapse cores. The Lattimer-Swesty EOS with incompressibility parameter $K = 180$ MeV [55] and the Shen EOS with $K = 281$ MeV [56,57] are also used. As the simulations are axisymmetric, the waveform catalog is linearly polarized. A representative waveform from the Dimmelmeier *et al.* catalog is shown in the top panel of Fig. 1. As the main feature of the Dimmelmeier waveforms is the spike at core bounce, they are still a good approximation of a 3D CCSNe signal as any rotating model likely stays sufficiently close to axisymmetry around the bounce and the bounce signal is still clearly present in 3D magnetorotational waveforms.

Sample waveforms are also drawn from the following rotating core-collapse simulations:

(i) Scheidegger *et al.* [59] carried out 3D magnetohydrodynamical simulations, using a leakage scheme for neutrino transport. These were performed with a 15 $M_\odot$ progenitor star, and the Lattimer-Swesty EOS with $K = 180$ MeV [55]. Due to the 3D nature of the simulations, the Scheidegger *et al.* waveforms have two polarizations. We employ waveforms from models R3E1AC$_{\rm L}$ (moderate precollapse rotation, toroidal/poloidal magnetic field strength of 10^6 G/10^9 G) shown in Fig. 2 and R4E1FC$_{\rm L}$ (rapid precollapse rotation, toroidal/poloidal magnetic field strength of 10^{12} G/10^9 G). We hereafter refer to these waveforms as `sch1` and `sch2`, respectively.

(ii) Abdikamalov *et al.* [52] performed axisymmetric general-relativistic hydrodynamics simulations. A 15 $M_\odot$ progenitor star was used, and the Lattimer-Swesty EOS with $K = 220$ MeV was employed [55]. We use waveforms from models *A*1*O*14 ($A = 300$ km; $\Omega_c = 14$ rad s^{-1}), *A*3*O*09 ($A = 634$ km; $\Omega_c = 9$ rad s^{-1}), and *A*4*O*01 ($A = 1268$ km; $\Omega_c = 1$ rad s^{-1}). We hereafter refer to these waveforms as `abd1`, `abd2`, and `abd3`, respectively.

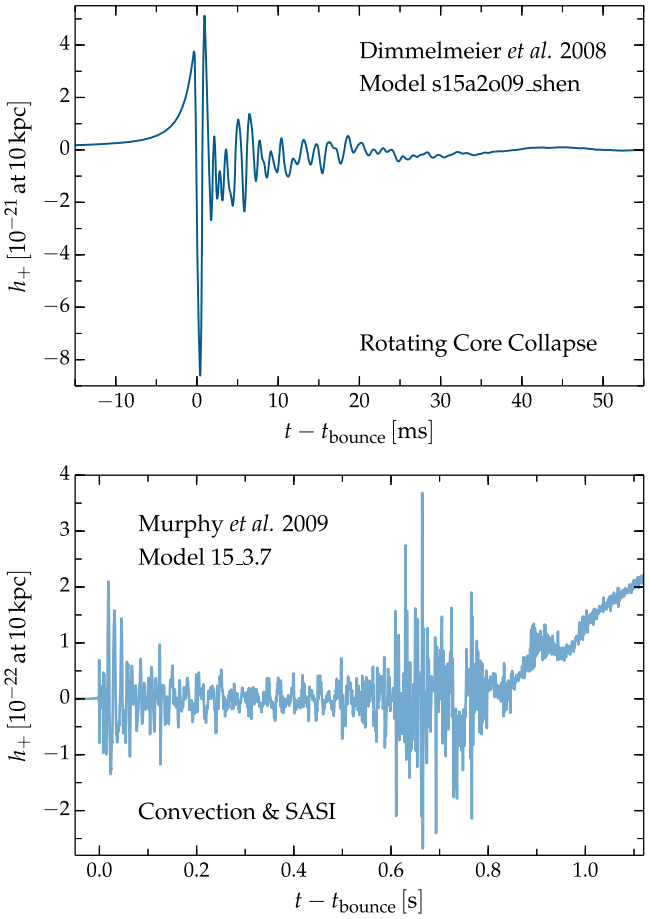

FIG. 1. Time domain GW strain for representative models of rotating core collapse (top panel) and neutrino-driven (bottom panel), as seen by an equatorial observer at 10 kpc, drawn from the RotCC and C&S waveform catalogs, respectively [51,58]. We note that the typical GW strain from rotating core collapse is roughly an order of magnitude larger than the typical GW strain from neutrino-driven explosions. In addition, the typical GW signal duration is roughly an order of magnitude longer for neutrino-driven explosions than for rotating core collapse.

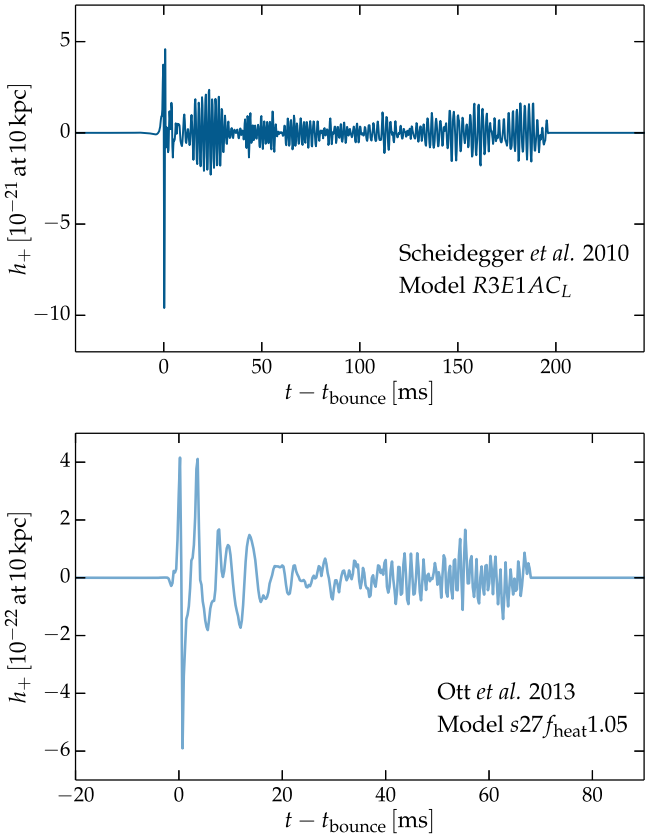

FIG. 2. Time domain h_+ GW strain for representative 3D models of rotating core collapse (top panel) and neutrino-driven convection (bottom panel), as seen by an equatorial observer at 10 kpc, drawn from the Scheidegger *et al.* [59] and Ott *et al.* [35] waveform catalogs.

B. Neutrino mechanism

During the collapse of the iron core, and subsequent evolution of the protoneutron star to a cold neutron star, approximately 3×10^{53} erg of energy is released, and 99% of this energy is transported out by neutrinos [3]. The neutrino mechanism theorizes that if some small fraction of the energy emitted in neutrinos were reabsorbed behind the stalled accretion shock, shock heating could reenergize the shock and drive an explosion. In its early form, the neutrino mechanism was first proposed by Arnett [60], and Colgate and White [61], while the modern form of the mechanism was put forward by Bethe and Wilson [62].

The GW signal from neutrino-driven CCSNe is dominated by contributions from turbulent convection and the SASI [36,63–66]. Immediately after bounce, there is a burst of GWs from prompt convection [10], which is driven by the negative entropy gradient set up by the stalled shock. The GW emission dies down as the entropy gradient smooths out but strengthens as the SASI becomes nonlinear on time scales of several 100 ms. Accretion plumes are rapidly decelerated as they enter the region behind the shock, leading to numerous spikes in the GW signal [58]. The GW signal is broadband in frequency, with most emission between 100 and 1100 Hz. The signal typically lasts from ∼0.3–2 s, with strain $\sim 10^{-22}$ for a source at 10 kpc. The total $E_{\rm GW}$ from neutrino-driven explosions are of order $10^{-11} - 10^{-9} M_\odot$.

1. GW waveform catalogs

In this study, we use the waveform catalog from Murphy *et al.* [58] to construct the neutrino mechanism PCs, hereafter referred to as the C&S model. The catalog is comprised of 16 waveforms, extracted using the quadrupole approximation [67], from axisymmetric Newtonian CCSN simulations. Electron capture and neutrino leakage are treated using a parametrized scheme, and only the

monopole term of the gravitational potential is included. The progenitor models considered are nonrotating and span the parameter space of ZAMS mass ($M_{\mathrm{ZAMS}} = \{12, 15, 20, 40\} M_{\odot}$) and total electron/antielectron neutrino luminosity. Due to the axisymmetric nature of the simulations, the waveforms extracted are linearly polarized. While the nature of the turbulent convection driving such explosions is expected to be very different in two and three dimensions, broad catalogs of waveforms extracted from 3D simulations have not yet been produced due to computational limitations. A representative waveform from the Murphy *et al.* catalog is shown in the bottom panel of Fig. 1, for a source at 10 kpc.

Sample waveforms are drawn from the following nonrotating core collapse simulations:

(i) Yakunin *et al.* [68] carried out axisymmetric Newtonian simulations, using an approximate general relativity monopole term of the gravitational potential and including radiation hydrodynamics. We choose waveforms obtained from the simulation of a 15 $M_{\odot}$ progenitor star referred to as `yak`. Due to axisymmetry, the extracted waveform is linearly polarized.

(ii) Müller *et al.* [69] performed 3D simulations of neutrino-driven CCSNe with gray neutrino transport and an inner boundary condition to prescribe the contraction of the protoneutron star core. They started the simulations after core bounce and assumed a time-varying inner boundary, cutting out much of the protoneutron star. With the excised core, the signal from prompt convection cannot be captured in these models. Protoneutron star convection only contributes to their waveforms at late times, and the contraction of the protoneutron star lowers the GW frequency. As the simulations are 3D, the Müller *et al.* waveforms have two polarizations. We use waveform models L15-3 and W15-4 (both with a 15 $M_{\odot}$ progenitor) and model N20-2 (with a 20 $M_{\odot}$ progenitor) and refer to these waveforms as `müller1`, `müller2`, and `müller3`, respectively.

(iii) Ott *et al.* [35] performed 3D simulations of neutrino-driven CCSNe. The simulations are general relativistic and incorporate a three-species neutrino leakage scheme. As the simulations are 3D, the Ott *et al.* waveforms have two polarizations, and we use the GW waveform from model $s27f_{\mathrm{heat}}1.05$ (a 27 $M_{\odot}$ progenitor) shown in Fig. 2. We hereafter refer to this waveform as `Ott`.

III. SMEE

SMEE is designed as a parameter estimation follow-up analysis for possible detection candidates identified by GW burst searches. This section gives a brief overview of the Bayesian data analysis strategy implemented in SMEE. PCA via singular value decomposition (SVD) is applied to the catalog waveforms to create signal models that represent each explosion mechanism. Similar techniques have been used to extract physical parameters of GW signals from binary systems [70–72] and in characterizing noise sources in GW detectors [73,74].

In the previous SMEE analysis, a MATLAB implementation of SMEE was used, which has now been replaced with a faster and more accurate C implementation that is part of the LIGO data analysis software package LSC Algorithm Library [75]. In particular, we use the LALInference package [76–78], which is designed for the parameter estimation of GW signals.

A. Principal component analysis

PCA can be used to transform waveforms contained in a catalog into a set of orthogonal basis vectors called principal components. The first few PCs represent the main features of a set of waveforms, therefore allowing for a dimensional reduction of the data set. Before applying PCA, waveforms from the `RotCC` model are zero padded and aligned at the spike at core bounce. The `C&S` waveforms are aligned at the onset of emission. By applying SVD to the original data matrix D, where each column corresponds to a supernova waveform, the data can be factored such that

$$D = U\Sigma V^{\mathrm{T}}, \tag{2}$$

where U and V are matrices of which the columns are comprised of the eigenvectors of DD^{T} and $D^{\mathrm{T}}D$, respectively. Σ is a diagonal matrix with elements that correspond to the square root of the eigenvalues. The orthonormal eigenvectors in U are the PCs. As the PCs are ranked by their corresponding eigenvalues in Σ, the main features of the data set are contained in just the first few PCs. Each waveform, h_i, in the data set can be reconstructed using a linear combination of the PCs, multiplied by their corresponding PC coefficients $\beta = \Sigma V^{\mathrm{T}}$, such that

$$h_i = A \sum_{j=1}^{k} U_j \beta_j, \tag{3}$$

where A is an amplitude scale factor and k is the number of PCs. Bayesian model selection can then be applied to the signal models.

B. Bayesian model selection

Bayesian model selection is used to calculate Bayes factors that allow us to distinguish between two competing models. The Bayes factor, $B_{S,N}$, is given by the ratio of the evidences,

$$B_{S,N} = \frac{p(D|M_S)}{p(D|M_N)}, \tag{4}$$

where M_S and M_N are the signal and noise models, respectively. The evidence is given by the integral of the likelihood multiplied by the prior across all parameter values. For a large number of parameters, the evidence integral can become difficult. This problem is solved using a technique known as nested sampling. A detailed description of nested sampling is given in L12 and elsewhere [28,76].

For convenience, we take the logarithm of the Bayes factor,

$$\log B_{S,N} = \log[p(D|M_S)] - \log[p(D|M_N)]. \tag{5}$$

If $\log B_{S,N} > 0$, the signal model is preferred over the noise model. Conversely, if $\log B_{S,N} < 0$, the noise model is preferred over the signal model. In this same way, the evidence for two different explosion models, RotCC and C&S, can be compared as

$$\log B_{\mathrm{RotCC-C\&S}} = \log B_{\mathrm{RotCC},N} - \log B_{\mathrm{C\&S},N}. \tag{6}$$

Uniform priors are applied to each PC coefficient, with prior ranges set by the catalog waveforms padded by $\pm 10\%$ to account for uncertainty due to the lack of available waveforms, and a uniform-in-volume prior is applied to the amplitude parameter as it scales with distance. A full description of the likelihoods used is given in L12.

A galactic supernova (SN) will have coincident EM and neutrino signals, ensuring that the sky location of the target source will be known. Online searches for GW bursts can also produce sky maps of the location of the GW signal [77]. For this reason, we fix the sky location of the source as a known parameter.

C. Number of PCs

Previously in L12, the relative complexity of the RotCC and C&S models was not taken into consideration when selecting the number of PCs.

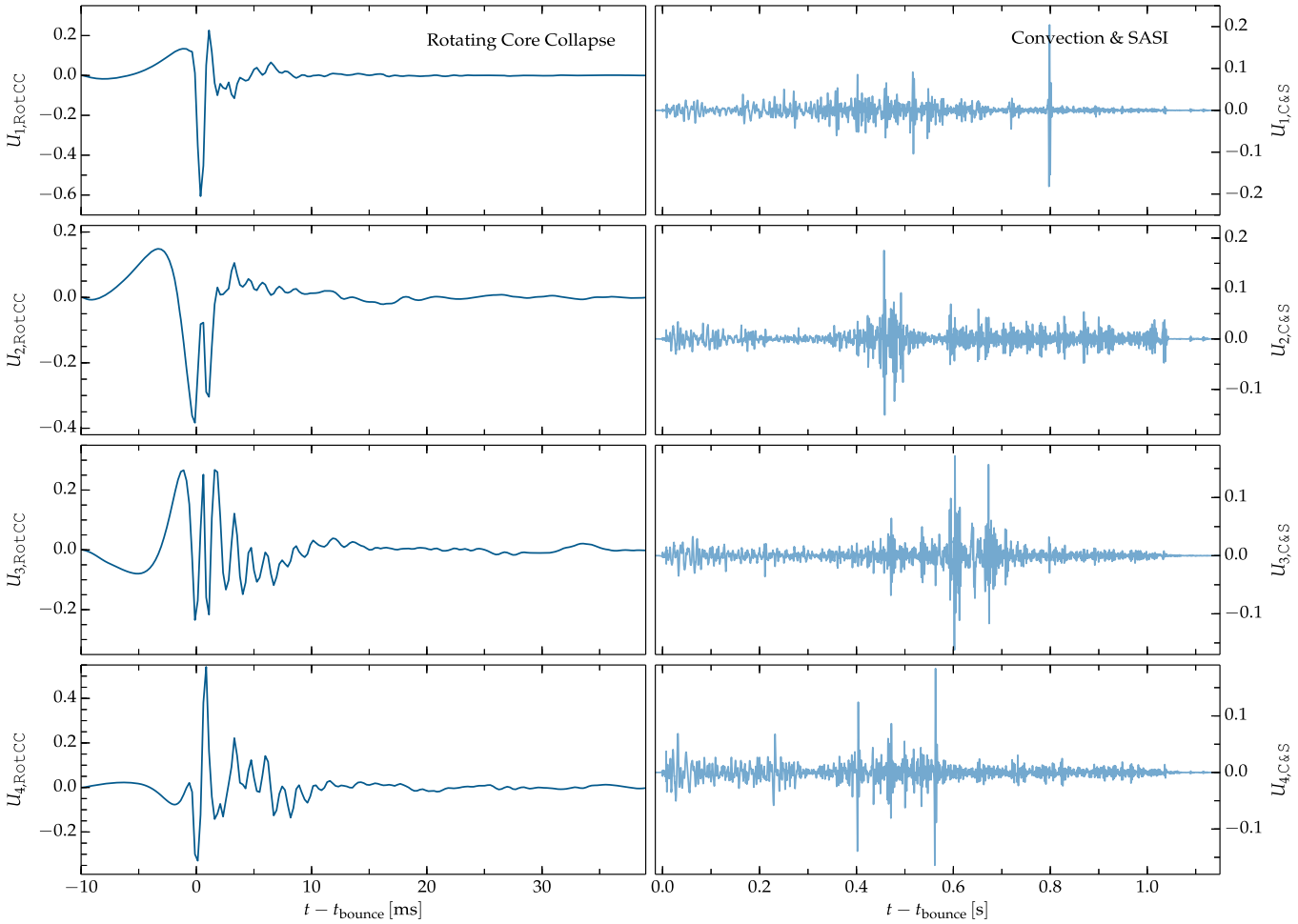

FIG. 3. (Left) The first four PCs for the RotCC model. (Right) As for the left, but for the C&S model. The first few PCs represent the most common features of the waveforms used in the analysis. A larger number of PCs is needed to represent the broad set of features in waveforms from the C&S model. The main feature of the RotCC model PCs is the spike at core bounce.

Figure 3 shows the first four PCs for the RotCC and C&S models. It is clear that the time domain structure of the C&S model is far more complex than that for the RotCC model. Due to this, fewer RotCC PCs are typically needed to faithfully reconstruct GW signals from rotating core collapse than the number of C&S PCs needed to reconstruct GW signals from neutrino-driven CCSNe. To account for this, we aim to quantify the impact of the number of PCs for each model.

This is typically achieved by studying the variance encompassed by each PC and using the number of PCs that cumulatively contain above some fraction of the total variance [73,79]. However, as this method only uses the waveforms, it does not account for the limitations of the analysis method implemented in SMEE. Bayesian model selection favors simpler models, and this could increase errors when results are more uncertain, such as when the signal to noise ratio (SNR) of the GW signal is low [28]. To this end, we determine the optimal number of PCs from the behavior of $\log B_{S,N}$ for both models across the waveform catalogs.

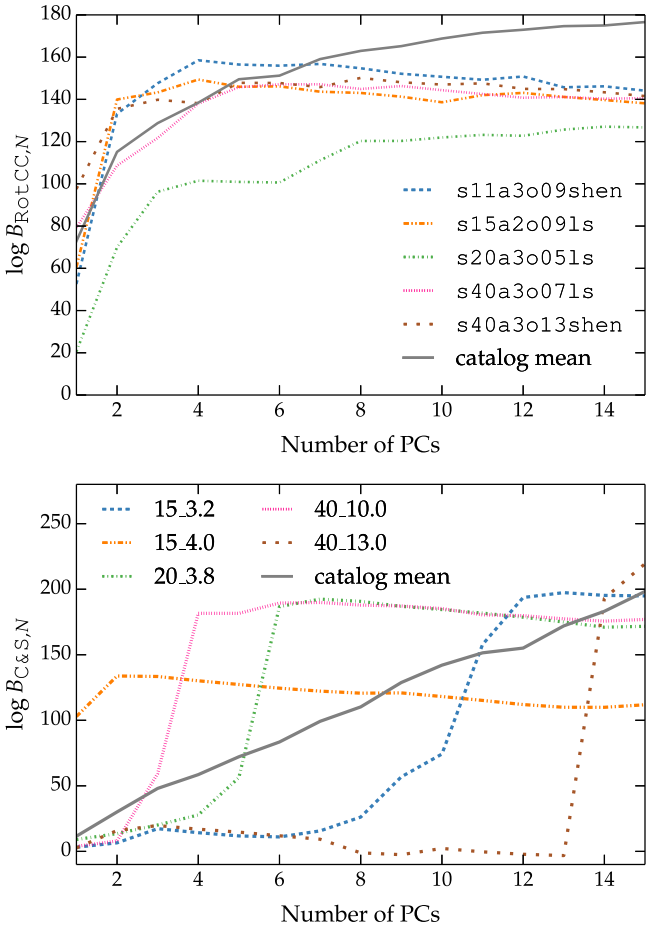

FIG. 4. The log $B_{S,N}$ values for an increasing number of PCs for the RotCC (top panel) and C&S (bottom panel) models using five representative waveforms from each mechanism. Log $B_{S,N}$ increases as more PCs are added and more information is gained about the injected signal. Log $B_{S,N}$ will decrease if the model becomes too complex.

In Fig. 4, we show $\log B_{S,N}$ for five representative waveforms from the RotCC and C&S models, which span the parameter space of the catalogs. We inject all of the signals with a SNR of 20, as $\log B_{S,N}$ is also proportional to the SNR of the signal. Larger SNRs produce larger values of $\log B_{S,N}$. As the number of PCs is increased, the model becomes a better match for the signal in the data, and $\log B_{S,N}$ increases sharply. After an ideal number of PCs is reached, no further information about the signal is gained by adding more PCs, and $\log B_{S,N}$ stops increasing. If more PCs are added after the ideal number, then $\log B_{S,N}$ will begin to decrease due to an Occam factor that occurs as the signal model becomes too complex.

The waveforms in the RotCC catalog have a small variance, and therefore a small number of PCs are needed to represent the entire catalog. The C&S model has greater variance in the catalog waveforms, and a larger number of PCs are required to accurately represent all the features included in all waveforms. We select six PCs for the RotCC model and nine PCs for the C&S model to maximize the number of features represented in the PCs while minimizing the penalty that occurs when the model is too complex or one model is significantly more complex than the other.

IV. ANALYSIS

In L12, simulated Gaussian noise was considered in a single aLIGO detector in the context of a sky position where antenna sensitivity to linearly polarized GW signals was maximized. For this study, SMEE has been extended to incorporate a three detector network, which consists of the two aLIGO detectors and the AdVirgo detector, hereafter referred to as H1, L1, and V1, respectively.

Real data from GW detectors are nonstationary and non-Gaussian, and, as such, it is important to test our analysis in real nonstationary, non-Gaussian noise. We use the observational data taken by H1 and L1 during the S5 science run and data taken by V1 during the VSR1 science run, which are now publicly available via the LIGO Open Science Center [80]. These data are recolored to the design sensitivity PSD of aLIGO and AdVirgo, as outlined in Ref. [14], which permits a more realistic estimation of the sensitivity of our analysis in future advanced detector observation runs. The detectors are expected to reach design sensitivity in 2019.

The antenna response of the detectors is periodic with an associated time scale of one sidereal day, due to the rotation of the Earth. As a consequence of this, the sensitivity of any GW analysis using stretches of data much shorter than this time scale is strongly dependent on the antenna

response of the detectors to the source location at the relevant GPS time. To represent the time-averaged sensitivity of the detector network, we choose ten GPS times spread throughout a 24 h period.

V. RESULTS

A. Response to noise

The response of SMEE to instances of simulated Gaussian noise was investigated in L12 to better understand the results in the presence of real signals. As SMEE is now implemented in C, and the relative complexity of the waveforms is now accounted for in the number of PCs, we recalculate the noise response using 1000 instances of simulated aLIGO and AdVirgo design sensitivity noise.

In Fig. 5, $\log B_{S,N}$ for 1000 instances of Gaussian and real nonstationary, non-Gaussian noise is shown.

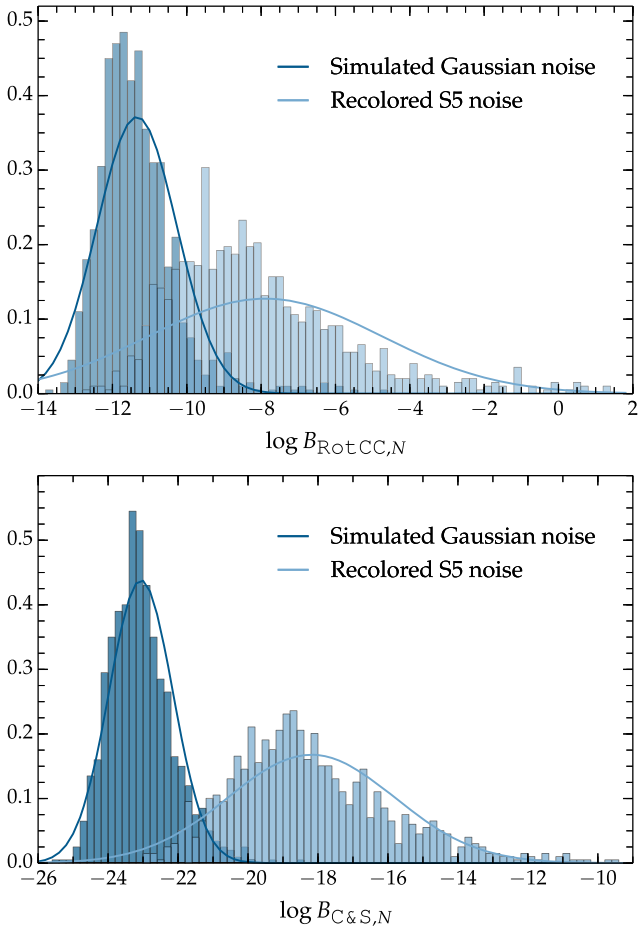

FIG. 5. Response of SMEE to 1000 instances of simulated and recolored aLIGO and AdVirgo design sensitivity noise for RotCC with six PCs (top panel) and C&S with nine PCs (bottom panel). Transient noise artifacts and lines in the real data can increase log $B_{S,N}$ and the standard deviation of the noise response.

The $\log B_{S,N}$ values are obtained by running SMEE on 1000 GPS times, during the 24 h period of data, which contains no GW signals. The mean values are −12 for the RotCC model and −23 for the C&S model in Gaussian noise and −9 for the RotCC model and −19 for the C&S model in the recolored noise. Short duration transient noise artifacts and lines in the data increase SMEE's response to noise and increase the standard deviation of the noise response. In L12, a threshold value of 5 on $\log B_{S,N}$ was set using the standard deviation of the noise response. We increase the threshold on the value of $\log B_{S,N}$ to 10 to account for the increased variation in the noise response found in the real non-Gaussian data.

B. Determining the core-collapse supernova explosion mechanism

To test SMEEs ability to determine the explosion mechanism, all 128 RotCC and 16 C&S waveforms are injected at ten GPS times, giving a total of 1440 injected signals at each distance. The sky position of the Galactic center is used at distances of 2, 10, and 20 kpc to show how well the explosion mechanism can be determined for sources throughout the Galaxy.

Table I shows the antenna pattern averaged $\log B_{SN}$ for five representative waveforms from the RotCC and C&S models injected in recolored noise. How well SMEE can distinguish a signal from noise is important because the explosion mechanism cannot be determined for a signal it cannot detect. The table shows the mean $\log B_{S,N}$ is much larger for waveforms from the RotCC model as they have a larger SNR than the C&S waveforms. The

TABLE I. The mean $\log B_{S,N}$ for five representative waveforms from each mechanism injected at 2, 10, and 20 kpc at the sky position of the Galactic center. Waveforms from the RottCC model can be distinguished from noise throughout the Galaxy. C&S catalog waveforms at 20 kpc are indistinguishable from noise.

	$\log B_{\mathtt{RotCC},N}$			$\log B_{\mathtt{C\&S},N}$		
Waveform	2 kpc	10 kpc	20 kpc	2 kpc	10 kpc	20 kpc
RotCC						
s11a3o09_shen	24281	927	210	591	7	−8
s15a2o09_ls	27321	1050	241	785	15	−7
s20a3o05_ls	12151	447	92	1223	31	−3
s40a3o07_ls	54281	2121	508	1898	53	0
s40a3o13_shen	64323	2537	618	20510	815	192
C&S						
15_3.2	52	−4	−5	328	−6	−12
15_4.0	59	−4	−6	2982	90	5
20_3.8	69	−5	−5	1629	352	−8
40_10.0	20	−5	−6	1687	42	−4
40_13.0	21	−6	−6	24	−11	−12

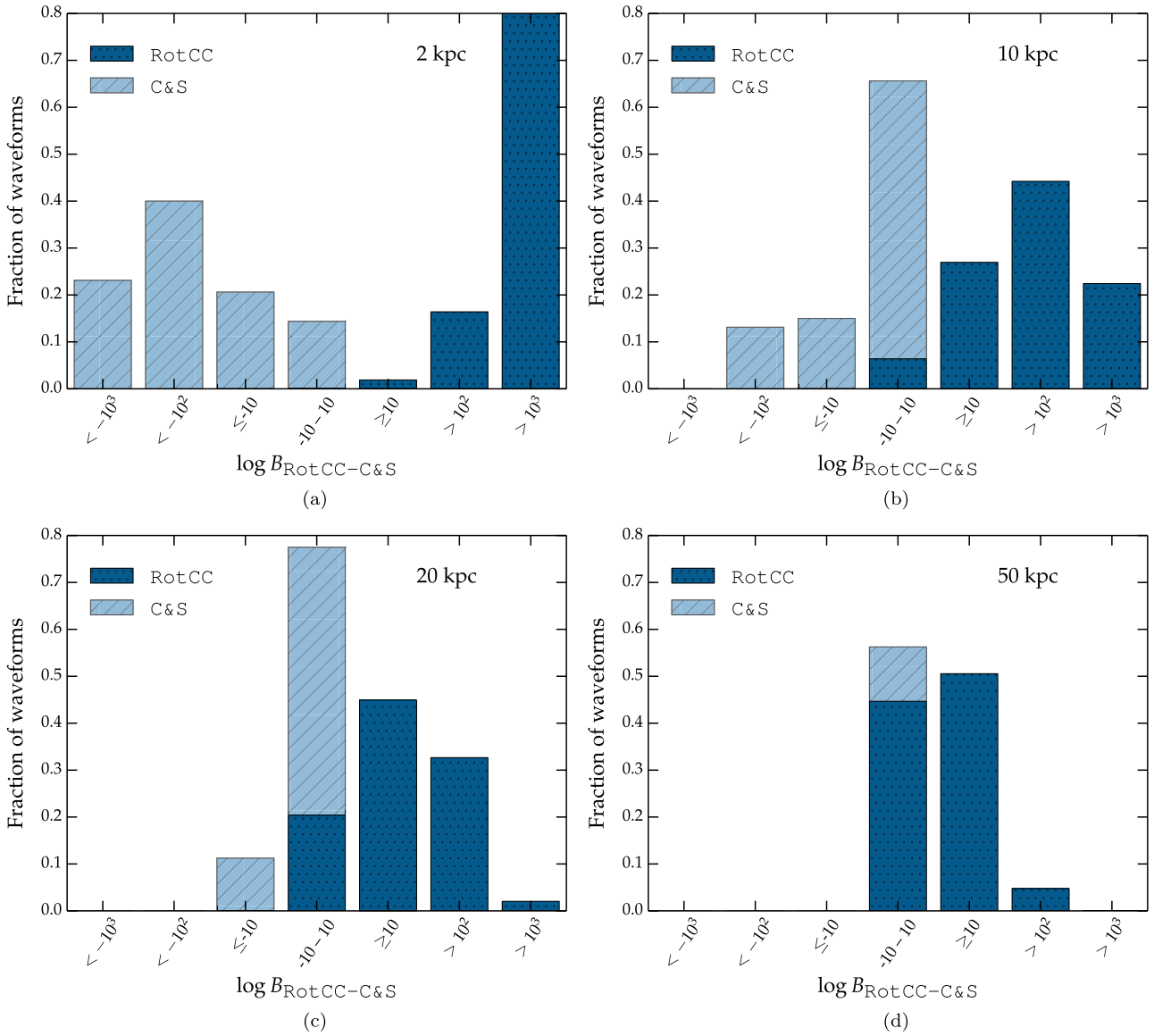

FIG. 6. Log $B_{\mathrm{RotCC-C\&S}}$ for waveforms injected from the RottCC and C&S catalogs. (a) At 2 kpc and the sky position of the Galactic center, the explosion mechanism is correctly determined for all 1437/1440 detected waveforms. (b) At 10 kpc 1198/1440, waveforms are detected, and their explosion mechanism is correctly determined. (c) Almost all the C&S waveforms have a SNR too small for them to be detected at 20 kpc. (d) Distance of 50 kpc and sky position of the Large Magellanic Cloud.

value of $\log B_{SN}$ should be larger when using the PCs from the correct explosion mechanism. Waveforms from the RotCC model can be distinguished from noise at all of the Galactic distances considered. Waveforms from the C&S model can all be distinguished from noise at 2 kpc.

Figure 6 shows histograms of $\log B_{\mathrm{RotCC-C\&S}}$ for all 1440 injections at three Galactic distances. If the RotCC waveforms are identified with the correct explosion mechanism, then $\log B_{\mathrm{RotCC-C\&S}}$ will be positive, and if the C&S waveforms are identified with the correct explosion mechanism, then $\log B_{\mathrm{RotCC-C\&S}}$ will be negative. If $\log B_{\mathrm{RotCC-C\&S}}$ is between -10 and 10, then either the injected waveform could not be distinguished from noise or it is not possible to distinguish between the explosion mechanisms considered.

The number of detected waveforms from the C&S model is 157/160, 150/160, and 19/160 at distances of 2, 10, and 20 kpc, respectively. The number of detected waveforms from the RotCC model is 1279/1280, 1198/1280, and 1019/1280 at distances of 2, 10, and 20 kpc, respectively. The correct explosion mechanism is determined for all detected waveforms from both models at all Galactic distances.

All catalog waveforms are then injected at the sky position of the Large Magellanic Cloud at a distance of 50 kpc at ten different GPS times. A histogram of $\log B_{\texttt{RotCC-C\&S}}$ is shown in Fig. 6(d). 707/1280 waveforms from the RotCC model can be distinguished from noise at this distance, and their explosion mechanism is correctly determined as magnetorotational. Waveforms injected from the C&S model cannot be distinguished from noise at a distance of 50 kpc.

C. Testing robustness using noncatalog waveforms

As the waveforms from the RotCC and C&S models used to create the PCs may not be an exact match for a real CCSN GW signal, it is important to test the robustness of the method applied in SMEE using waveforms that do not come from the catalogs used to construct the PCs. To test robustness, we use five extra waveforms from each mechanism. For the magnetorotational mechanism, the extra waveforms are sch1, sch2, and the three abd waveforms as described in Sec. II A 1. For the neutrino mechanism, the five extra waveforms are the yak, Ott, and three müller waveforms described in Sec. II B 1.

As for the RotCC and C&S waveforms, the ten extra waveforms are injected at ten GPS times at the sky position of the Galactic center at distances of 2, 10, and 20 kpc, leading to a total of 100 injections at each distance. Table II shows how well the extra waveforms can be distinguished from noise at the three Galactic distances considered. As for the catalog waveforms, the table shows the antenna pattern averaged values of $\log B_{S,N}$. A larger value of $\log B_{S,N}$ is expected when the correct PCs are used. The confidence in the result is larger for larger values of $\log B_{S,N}$. All the extra magnetorotational mechanism waveforms can be distinguished from noise at the three Galactic distances considered. The yak and Ott waveforms can be distinguished from noise at 2 kpc. The three müller waveforms cannot be distinguished from noise at any of the Galactic distances considered.

TABLE II. The mean $\log B_{S,N}$ for five extra waveforms representing each explosion mechanism injected at 2, 10, and 20 kpc at the sky position of the Galactic center. The three müller waveforms at 20 kpc are indistinguishable from noise. The extra magnetorotational mechanism waveforms can be distinguished from noise throughout our Galaxy.

	$\log B_{\texttt{RotCC},N}$			$\log B_{\texttt{C\&S},N}$		
Waveform	2 kpc	10 kpc	20 kpc	2 kpc	10 kpc	20 kpc
RotCC						
sch1	15116	567	124	2181	64	3
sch2	47185	1843	441	7369	321	69
abd1	87453	3454	843	21528	933	235
abd2	50420	2000	488	18128	798	183
abd3	6426	247	55	5147	185	31
C&S						
yak	23	−5	−6	141	−10	−11
müller1	−5	−5	−5	−9	−12	−11
müller2	−5	−6	−5	−8	−10	−12
müller3	−5	−5	−6	−9	−11	−11
Ott	118	−2	−6	24	−12	−12

Figure 7 shows histograms of $\log B_{\texttt{RotCC-C\&S}}$ for all 100 extra waveform injections at distances throughout the Galaxy. As for the waveforms used to calculate the PCs, if the explosion mechanism of the magnetorotational waveforms is correctly determined, then $\log B_{\texttt{RotCC-C\&S}}$ will be positive, and if the explosion mechanism of the neutrino mechanism waveforms is correctly determined, then $\log B_{\texttt{RotCC-C\&S}}$ will be negative. At all distances, the 30 injected müller waveforms cannot be distinguished from noise. At 2 kpc, the explosion mechanism of the ten injected yak waveforms is correctly determined as neutrino driven. The explosion mechanism of the 10 Ott waveform injections are incorrectly determined as magnetorotational. The Ott waveforms, shown in Fig. 2, contain a feature during the first 20 ms that appears reminiscent of the rotational bounce signals. This is due to a strong signal from the early postbounce phase that arises because of artificially strong prompt convection induced by the neutrino leakage scheme. This feature is likely the cause of the incorrect result. If larger catalogs of 3D CCSN waveforms are obtained, then PCs containing both polarizations could be used to improve results for any waveforms that are currently poorly reconstructed by SMEE. All extra magnetorotational mechanism injections at 2 kpc are distinguished from noise, and their explosion mechanism is correctly determined.

At 10 kpc, 1/10 yak injections and 49/50 magnetorotational injected waveforms can be distinguished from noise. The explosion mechanism is correctly determined for all detected waveforms. At 20 kpc, 45/50 magnetorotational waveforms and none of the extra neutrino mechanism waveforms can be distinguished from noise. The explosion mechanism is correctly determined for all detected magnetorotational waveforms at 20 kpc.

Figure 7(d) shows a histogram of $\log B_{\texttt{RotCC-C\&S}}$ for 100 injections of the extra waveforms at 50 kpc at the sky position of the Large Magellanic Cloud. 27/50 magnetorotational waveforms can be distinguished from noise, and their explosion mechanism is correctly determined as magnetorotational.

VI. SUMMARY AND DISCUSSION

SMEE is designed to measure astrophysical parameters of a CCSN GW detection. CCSNe have long been considered as a potential source for an aLIGO and

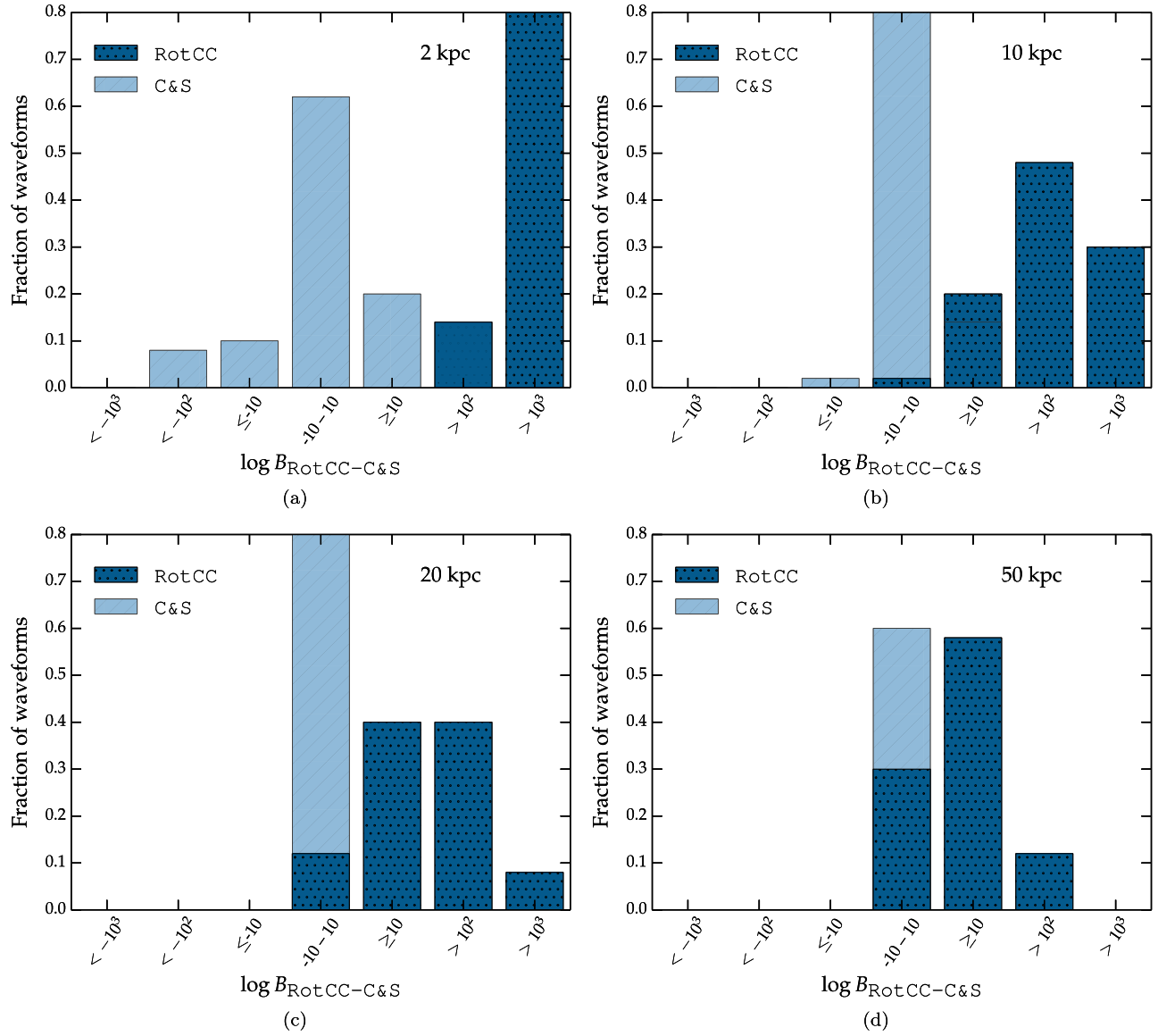

FIG. 7. Log $B_{\mathrm{RotCC-C\&S}}$ for five extra waveforms representing each explosion mechanism. (a) At 2 kpc, all extra magnetorotational mechanism waveforms can be distinguished from noise, and their explosion mechanism is correctly determined. For the extra neutrino mechanism waveforms, only the explosion mechanism of the `yak` waveform is correctly determined. (b) At 10 kpc, all extra neutrino mechanism waveforms cannot be distinguished from noise. (c) At 20 kpc, 45/100 injected extra magnetorotational waveforms can be distinguished from noise, and their explosion mechanism is correctly determined. (d) The correct explosion mechanism is determined for all extra magnetorotational waveforms distinguishable from noise (27/100) at 50 kpc.

AdVirgo detector network, and a CCSN detection may provide an ideal probe of the inner regions of the explosion that do not emit electromagnetically. Determining the CCSN explosion mechanism is essential for a full understanding of the physics and processes involved in CCSNe.

For the first time, we demonstrate the ability of SMEE to determine the CCSN explosion mechanism with a network of GW detectors with real nonstationary and non-Gaussian noise. In this paper, SMEE considers the magnetorotational and neutrino explosion mechanisms and shows how the correct explosion mechanism can be determined for all detectable catalog waveforms at distances throughout our Galaxy. GW signals from neutrino-driven convection have a smaller amplitude than those from rapidly rotating core collapse, and therefore detections at distances of 10 kpc or less are needed for a robust result. Furthermore, we can determine the explosion mechanism of rapidly rotating core-collapse waveforms at the distance and sky position of the Large Magellanic Cloud.

We further enhance the model selection capabilities of SMEE with a careful selection of the number of PCs that considers the relative complexity of the different explosion models. A large number of PCs is required to represent all

the common features of the neutrino-driven convection waveforms. The number of available waveforms is much smaller than those available for rapidly rotating core collapse, and the differences between individual waveforms is much larger. This leads to a reduction in the robustness of the result from SMEE as the parameter space of the neutrino waveforms is not sufficiently covered. Furthermore, 3D neutrino waveforms contain some features that are different from the 2D waveforms used to create the PCs. However, the 2D rapidly rotating core-collapse waveforms are still a good approximation for 3D rapidly rotating waveforms as nonaxisymmetric instabilities occur after the signal bounce that is the main feature in the rapidly rotating PCs.

During recent years, 2D neutrino mechanism waveforms with more detailed physics have become available. They include an updated version of the `yak` waveforms used in this study, which are now complete (up to 1 s) waveforms, as the 2010 waveforms were truncated at ∼500 ms after bounce [81]. Waveforms produced by Müller *et al.* (2013) [82] are the first 2D CCSNe relativistic GW signals with multigroup, three-flavor neutrino transport. Furthermore, a larger number of 3D neutrino mechanism waveforms have become available recently, including Kuroda *et al.* (2016) [36], who simulate a 15 $M_\odot$ star with three different EOSs showing a strong low-frequency signal from the SASI, and Andresen *et al.* (2016) [40], who include multigroup neutrino transport. Updating SMEE to use these 3D waveforms, as well as other 3D waveforms for rapidly rotating CCSNe (e.g. Kuroda *et al.* [41]), will be essential for future robust parameter estimation with CCSNe GWs.

Future work for SMEE will include following up real GW triggers found in the searches for GWs as it is possible that a real trigger may not belong to any of the models considered by SMEE. Therefore, future work for SMEE will include distinguishing an astrophysical CCSN explosion mechanism signal from other GW signal types and noise transients. Spectrograms or power spectra may be used instead of the Fourier transform of the time series waveforms to remove the models reliance on phase. How well SMEE can reconstruct the detected GW signal will also be explored in future studies. This can be compared with other tools that reconstruct GW waveforms using minimal assumptions about the signal morphology [83–85].

ACKNOWLEDGMENTS

The authors acknowledge helpful exchanges with James Clark, Alan Weinstein, Jonah Kanner, Rory Smith, and the LIGO SN working group that have benefitted this paper. We thank the CCSN simulation community for making their gravitational waveform predictions available for this study. I. S. H., J. P., and J. L. are supported by UK Science and Technology Facilities Council Grants No. ST/L000946/1 and No. ST/L000946/1. The authors also gratefully acknowledge the support of the Scottish Universities Physics Alliance. LIGO was constructed by the California Institute of Technology and Massachusetts Institute of Technology with funding from the National Science Foundation and operates under cooperative Agreements No. PHY-0107417 and No. PHY-0757058.

[1] W. Baade and F. Zwicky, *Proc. Natl. Acad. Sci. U.S.A.* 20, 259 (1934).
[2] E. Baron and J. Cooperstein, Astrophys. J. **353**, 597 (1990).
[3] H. A. Bethe, Rev. Mod. Phys. **62**, 801 (1990).
[4] E. O'Connor and C. D. Ott, Astrophys. J. **730**, 70 (2011).
[5] H.-T. Janka, Annu. Rev. Nucl. Part. Sci. **62**, 407 (2012).
[6] T. Foglizzo *et al.*, Publ. Astron. Soc. Aust. **32**, e009 (2015).
[7] K. Hirata, T. Kajita, M. Koshiba, M. Nakahata, and Y. Oyama, Phys. Rev. Lett. **58**, 1490 (1987).
[8] R. M. Bionta, G. Blewitt, C. B. Bratton, D. Casper, and A. Ciocio, Phys. Rev. Lett. **58**, 1494 (1987).
[9] R. Schaeffer, Y. Declais, and S. Jullian, Nature (London) **330**, 142 (1987).
[10] C. D. Ott, Classical Quantum Gravity **26**, 063001 (2009).
[11] K. Kotake, K. Sato, and K. Takahashi, Rep. Prog. Phys. **69**, 971 (2006).
[12] G. M. Harry *et al.* (LIGO Scientific Collaboration), Classical Quantum Gravity **27**, 084006 (2010).
[13] F. Acernese *et al.*, Classical Quantum Gravity **32**, 024001 (2015).
[14] S. E. Gossan, P. Sutton, A. Stuver, M. Zanolin, K. Gill, and C. D. Ott, Phys. Rev. D **93**, 042002 (2016).
[15] S. van den Bergh and G. A. Tammann, Annu. Rev. Astron. Astrophys. **29**, 363 (1991).
[16] E. Cappellaro, M. Turatto, S. Benetti, D. Y. Tsvetkov, O. S. Bartunov, and I. N. Makarova, Astron. Astrophys. **273**, 383 (1993).
[17] E. N. Alexeyev and L. N. Alexeyeva, J. Exp. Theor. Phys. **95**, 5 (2002).
[18] K. Gill, M. Branchesi, M. Zanolin, and S. M. Szczepanczyk (unpublished).
[19] B. P. Abbott *et al.* (LIGO Scientific and Virgo Collaborations), Phys. Rev. D **94**, 102001 (2016).
[20] B. J. Owen and B. S. Sathyaprakash, Phys. Rev. D **60**, 022002 (1999).
[21] J. Logue, C. D. Ott, I. S. Heng, P. Kalmus, and J. Scargill, Phys. Rev. D **86**, 044023 (2012).

[22] H.-T. Janka, K. Langanke, A. Marek, G. Martínez-Pinedo, and B. Müller, Phys. Rep. **442**, 38 (2007).
[23] A. Burrows, L. Dessart, E. Livne, C. D. Ott, and J. Murphy, Astrophys. J. **664**, 416 (2007).
[24] A. Burrows, E. Livne, L. Dessart, C. D. Ott, and J. Murphy, Astrophys. J. **640**, 878 (2006).
[25] A. Burrows, E. Livne, L. Dessart, C. D. Ott, and J. Murphy, Astrophys. J. **655**, 416 (2007).
[26] I. S. Heng, Classical Quantum Gravity **26**, 105005 (2009).
[27] C. Röver, M.-A. Bizouard, N. Christensen, H. Dimmelmeier, I. S. Heng, and R. Meyer, Phys. Rev. D **80**, 102004 (2009).
[28] D. S. Sivia, *Data Analysis, A Bayesian Tutorial* (Clarendon, Oxford, 1996).
[29] J. Skilling, TITLE, *American Institute of Physics Conference Series*, edited by R. Fischer, R. Preuss, and U. V. Toussaint (PUBLISHER, LOCATION, 2004), Vol. 735, p. 395.
[30] L. Wang and J. C. Wheeler, Annu. Rev. Astron. Astrophys. **46**, 433 (2008).
[31] R. Chornock *et al.*, Astrophys. J. **739**, 41 (2011).
[32] N. Smith *et al.*, Mon. Not. R. Astron. Soc. **420**, 1135 (2012).
[33] B. Sinnott, D. L. Welch, A. Rest, P. G. Sutherland, and M. Bergmann, Astrophys. J. **767**, 45 (2013).
[34] S. E. Boggs *et al.*, Science **348**, 670 (2015).
[35] C. D. Ott, E. Abdikamalov, P. Mösta, R. Haas, S. Drasco, E. P. O'Connor, C. Reisswig, C. A. Meakin, and E. Schnetter, Astrophys. J. **768**, 115 (2013).
[36] T. Kuroda, K. Kotake, and T. Takiwaki, Astrophys. J. Lett. **829**, L14 (2016).
[37] C. D. Ott, H. Dimmelmeier, A. Marek, H.-T. Janka, I. Hawke, B. Zink, and E. Schnetter, Phys. Rev. Lett. **98**, 261101 (2007).
[38] M. Shibata and Y.-I. Sekiguchi, Phys. Rev. D **71**, 024014 (2005).
[39] S. Scheidegger, T. Fischer, S. C. Whitehouse, and M. Liebendörfer, Astron. Astrophys. **490**, 231 (2008).
[40] H. Andresen, B. Mueller, E. Mueller, and H.-T. Janka, arXiv:1607.05199.
[41] T. Kuroda, T. Takiwaki, and K. Kotake, Phys. Rev. D **89**, 044011 (2014).
[42] K. Kotake, W. Iwakami-Nakano, and N. Ohnishi, Astrophys. J. **736**, 124 (2011).
[43] K. Kotake, W. Iwakami, N. Ohnishi, and S. Yamada, Astrophys. J. Lett. **697**, L133 (2009).
[44] K. Yakunin, P. Marronetti, O. B. Messer, A. Mezzacappa, E. J. Lentz, S. W. Bruenn, W. R. Hix, J. A. Harris, and J. M. Blondin, *American Astronomical Society Meeting Abstracts* (PUBLISHER, LOCATION, 2014), Vol. 223, p. 354.09.
[45] N. N. Weinberg and E. Quataert, Mon. Not. R. Astron. Soc. **387**, L64 (2008).
[46] C. D. Ott, A. Burrows, T. A. Thompson, E. Livne, and R. Walder, Astrophys. J. Suppl. Ser. **164**, 130 (2006).
[47] T. Takiwaki and K. Kotake, Astrophys. J. **743**, 30 (2011).
[48] A. Heger, S. E. Woosley, and H. C. Spruit, Astrophys. J. **626**, 350 (2005).
[49] T. Rembiasz, J. Guilet, M. Obergaulinger, P. Cerdá-Durán, M. A. Aloy, and E. Müller, Mon. Not. R. Astron. Soc. **460**, 3316 (2016).
[50] P. Mösta, C. D. Ott, D. Radice, L. F. Roberts, E. Schnetter, and R. Haas, Nature (London) **528**, 376 (2015).
[51] H. Dimmelmeier, C. D. Ott, A. Marek, and H.-T. Janka, Phys. Rev. D **78**, 064056 (2008).
[52] E. Abdikamalov, S. Gossan, A. M. DeMaio, and C. D. Ott, Phys. Rev. D **90**, 044001 (2014).
[53] S. Scheidegger, S. C. Whitehouse, R. Käppeli, and M. Liebendörfer, Classical Quantum Gravity **27**, 114101 (2010).
[54] M. Rampp, E. Mueller, and M. Ruffert, Astron. Astrophys. **332**, 969 (1998).
[55] J. M. Lattimer and F. Douglas Swesty, Nucl. Phys. **A535**, 331 (1991).
[56] H. Shen, H. Toki, K. Oyamatsu, and K. Sumiyoshi, Nucl. Phys. **A637**, 435 (1998).
[57] H. Shen, H. Toki, K. Oyamatsu, and K. Sumiyoshi, Prog. Theor. Phys. **100**, 1013 (1998).
[58] J. W. Murphy, C. D. Ott, and A. Burrows, Astrophys. J. **707**, 1173 (2009).
[59] S. Scheidegger, R. Käppeli, S. C. Whitehouse, T. Fischer, and M. Liebendörfer, Astron. Astrophys. **514**, A51 (2010).
[60] W. D. Arnett, Can. J. Phys. **44**, 2553 (1966).
[61] S. A. Colgate and R. H. White, Astrophys. J. **143**, 626 (1966).
[62] H. A. Bethe and J. R. Wilson, Astrophys. J. **295**, 14 (1985).
[63] J. M. Blondin, A. Mezzacappa, and C. DeMarino, Astrophys. J. **584**, 971 (2003).
[64] T. Foglizzo, P. Galletti, L. Scheck, and H.-T. Janka, Astrophys. J. **654**, 1006 (2007).
[65] T. Foglizzo, L. Scheck, and H.-T. Janka, Astrophys. J. **652**, 1436 (2006).
[66] L. Scheck, H.-T. Janka, T. Foglizzo, and K. Kifonidis, Astron. Astrophys. **477**, 931 (2008).
[67] C. W. Misner, K. S. Thorne, and J. A. Wheeler, *Gravitation* (Freeman, San Francisco, 1973).
[68] K. N. Yakunin *et al.*, Classical Quantum Gravity **27**, 194005 (2010).
[69] E. Müller, H.-T. Janka, and A. Wongwathanarat, Astron. Astrophys. **537**, A63 (2012).
[70] M. Pürrer, Classical Quantum Gravity **31**, 195010 (2014).
[71] J. Blackman, S. E. Field, C. R. Galley, B. Szilágyi, M. A. Scheel, M. Tiglio, and D. A. Hemberger, Phys. Rev. Lett. **115**, 121102 (2015).
[72] J. A. Clark, A. Bauswein, N. Stergioulas, and D. Shoemaker, Classical Quantum Gravity **33**, 085003 (2016).
[73] J. Powell, D. Trifirò, E. Cuoco, I. S. Heng, and M. Cavaglià, Classical Quantum Gravity **32**, 215012 (2015).
[74] J. Powell, A. Torres-Forné, R. Lynch, D. Trifirò, E. Cuoco, M. Cavaglià, I. S. Heng, and J. A. Font, arXiv:1609.06262.
[75] Ligo algorithm library, www.lsc-group.phys.uwm.edu/daswg/projects/lalsuite.html.
[76] J. Veitch *et al.*, Phys. Rev. D **91**, 042003 (2015).
[77] R. Essick, S. Vitale, E. Katsavounidis, G. Vedovato, and S. Klimenko, Astrophys. J. **800**, 81 (2015).

[78] R. Lynch, S. Vitale, R. Essick, E. Katsavounidis, and F. Robinet, arXiv:1511.05955.
[79] J. F. T. Hastie and R. Tibshirani, *The Elements of Statistical Learning* (Springer, Berlin, 2001).
[80] M. Vallisneri, J. Kanner, R. Williams, A. Weinstein, and B. Stephens, J. Phys. Conf. Ser. **610**, 012021 (2015).
[81] K. N. Yakunin *et al.*, Phys. Rev. D **92**, 084040 (2015).
[82] B. Müller, H.-T. Janka, and A. Marek, Astrophys. J. **766**, 43 (2013).
[83] N. J. Cornish and T. B. Littenberg, Classical Quantum Gravity **32**, 135012 (2015).
[84] S. Klimenko *et al.*, Phys. Rev. D **93**, 042004 (2016).
[85] S. Klimenko, I. Yakushin, A. Mercer, and G. Mitselmakher, Classical Quantum Gravity **25**, 114029 (2008).